

**Electrodynamics of Annealed and Unannealed
La_{0.66}Sr_{0.33}MnO₃ Thin Films**

A thesis submitted in partial fulfillment of the requirement
for the degree of Bachelor of Science in Physics from
The College of William and Mary

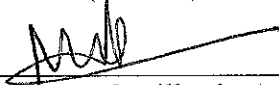
by

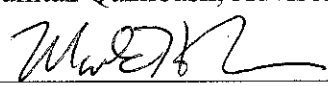
Daniel Robert Branagan

Accepted for

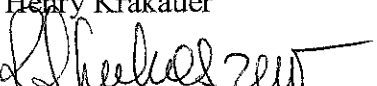
Honors

(Honors, No Honors)


Muntaz Qazilbash, Advisor


Mark Hinders


Henry Krakauer


R. Ale Lukaszew

Williamsburg, VA
April 26, 2012

Electrodynamics of Annealed and
Unannealed $\text{La}_{0.67}\text{Sr}_{0.33}\text{MnO}_3$ Thin Films

Daniel R. Branagan
Honors Thesis

Abstract

My project explored the impact of temperature and annealing on the optical constants of $\text{La}_{0.67}\text{Sr}_{0.33}\text{MnO}_3$ (LSMO) films grown on a lanthanum aluminate (LAO) substrate. This was done with infrared and optical spectroscopy, which allows us to measure the complex dielectric function of the material. Both the substrate and the film-substrate system have been modeled in order to closely examine the properties of annealed and unannealed LSMO. The Jahn-Teller energy splitting was measured, and an additional feature in the unannealed film conductivity allowed the Hund's coupling energy to be deduced directly.

I. Overview

The manganites, mixed metal oxides containing manganese, are a class of materials with particularly interesting properties, including colossal magnetoresistance, metal-insulator transitions, and charge ordering. These properties arise from strong electron-electron interactions, as well as electron-phonon and magnetic interactions.^{1,2,3}

A major source of complexity in this material is the atomic structure of manganese. In the d electron manifold, due to the crystal field the ground state splits as seen in Figure 1, with 3 electrons, denoted by the red arrows, in the lower t_{2g} levels and $(1 - x)$ electron in the higher e_g level. Here x is the strontium doping concentration, which in the case of LSMO is 0.33. When the e_g levels are singly occupied, as is the case in Mn^{3+} , this can cause a Jahn-Teller lattice distortion and therefore splits the e_g energy levels into two separated by an energy E_{JT} .

Due to the strong Coulomb repulsion, no d -orbital may be occupied by more than one electron, and due to Hunds-rule coupling, all electron spins on a given Mn ion must be ferromagnetically aligned. The electrons in the t_{2g} state form a core spin S_c with a magnitude $3/2$, while the electron in the e_g state can move freely if certain conditions are met. When an electron is on a site i , its spin must remain parallel with the associated S_c , and to move to position j , its spin must also be parallel with the S_c associated with the orbital. Therefore, in a ferromagnetic state with aligned spins throughout the material, the electrons will generally be delocalized. This phenomenon is known as “double exchange”.¹

As can be seen in Figure 3, the strontium-doped lanthanum manganates have a particularly complex phase diagram⁴ due to these interactions.

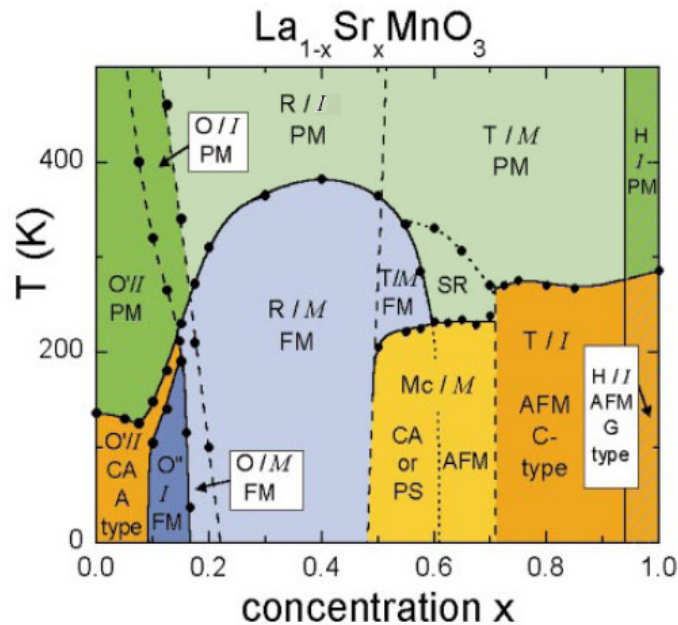


Figure 3: LSMO bulk phase diagram. While LaMnO_3 is an insulator at all temperatures, increasing the doping of strontium to $x=0.33$ causes a metal-insulator transition at $\sim 350\text{K}$. Adapted from a similar diagram in reference 4.

The base material LaMnO_3 is a Mott insulator at all temperatures, but at high temperatures it is paramagnetic, while at low temperatures it gains antiferromagnetic

properties. As the doping is increased further, at roughly $x=0.1$ this low temperature state remains an insulator but all spins become aligned; it is now ferromagnetic. Following that, in the $x=0.33$ concentration used here, the low temperature state becomes a ferromagnetic metal, and the high temperature state is a paramagnetic insulator.¹

This metal-insulator transition and a magnetic transition occur at a $T_c \approx 350\text{K}$ in bulk LSMO at $x=0.33$. One justification for these phase transitions is tied to double-exchange. In the high-temperature state the unaligned spins scatter electrons, while in the low-temperature ferromagnetic state the electron scattering rate decreases.¹ However, according to Millis this is insufficient, and the localization of electrons in the insulating phase is likely caused primarily by couplings between the lattice phonons and electrons¹. The localization would further prevent movement of electrons, but at lower temperatures would be overcome by the ferromagnetic order and thus the material would act as a metal.

Another important effect seen is phase separation. One might expect a homogenous film undergoing a metal to insulator phase transition to do so relatively rapidly around T_c , but in real data this is observed to be more gradual. This gradual transition, according to Becker et. al., is due to the formation of inherent inhomogeneities that arise from a phase separation, where domains of the insulating phase gradually appear and overwhelm the metallic phase, rather than the entire film making the transition abruptly.⁵ Therefore, even at temperatures below T_c portions of the material are in an insulating phase, and these areas grow with temperature.

Annealing the sample will change the oxygen content. As-grown films have an oxygen deficiency; when oxygen is absorbed into the lattice during the annealing process, this causes more Mn^{3+} ions to transition to Mn^{4+} , which will have an effect similar to

doping with Sr^{2+} . However, oxygen deficiency also has additional effects that are not caused by strontium. For example, absence of the oxygen ions will increase the c-axis lattice parameter. In the oxygen-deficient lattice, oxygen will no longer be present in the stoichiometric quantity O_3 , but instead will be in some quantity $\text{O}_{3-\delta}$. Annealing has been observed to have significant effect on the magnetic properties of the material, and may therefore also influence the electronic properties.⁶ Specifically, the complex dielectric function, which describes the dynamics of the charges in the material, should be examined around the metal-insulator transition for annealed and unannealed samples.

It has been shown in the past that as oxygen content increases, as it would be expected to in an annealed film, the metal-insulator transition temperature T_c shifts to higher temperatures⁷, and additionally the resistivity at low temperature decreases⁸. These changes likely come from how the change in oxygen content (and thus Mn^{4+} ion concentration) changes the carrier concentration, as well as the strain and disorder. These all provide further motivation for comparing the properties of annealed and unannealed LSMO.

The complex dielectric function, $\hat{\epsilon}(\omega) = \epsilon_1(\omega) + i\epsilon_2(\omega)$, encodes how electrons move in a solid, and is therefore closely linked to the electronic band structure and the electronic interactions in the material. Specifically, the real part ϵ_1 relates to the polarizability of the material, and the imaginary part ϵ_2 refers to the absorption. The complex conductivity $\hat{\sigma} = \sigma_1 + i\sigma_2$, can be related to the complex dielectric function by using the following formulas: (in Gaussian units)

$$\sigma_1 = \frac{\omega\epsilon_2(\omega)}{4\pi} \quad (1)$$

$$\sigma_2 = \frac{\omega(1 - \varepsilon_1(\omega))}{4\pi} \quad (2)$$

The aim of this project was to measure the frequency-dependent complex dielectric function ($\varepsilon_1(\omega)$ and $\varepsilon_2(\omega)$) of two $\text{La}_{0.67}\text{Sr}_{0.33}\text{MnO}_3$ thin films of 85nm thickness, grown via pulsed laser deposition onto an LAO substrate, and to examine how the dielectric function changes with temperature and with oxygen content. Both films had an orientation of [002], which was obtained via x-ray diffraction. One sample was annealed in an O_2 atmosphere to reduce oxygen deficiency, while the other was left unannealed. Temperature measurements were taken between room temperature ($\sim 300\text{K}$) and 400K, while the effects of the change in oxygen content were examined by using measurements on both the annealed and unannealed films.

I.1 Ellipsometry

Ellipsometry is an optical measurement technique that can be used to obtain the complex dielectric function. What it measures directly are Ψ and Δ , which are related to the ratio of the Fresnel coefficients for s and p -polarized light, \tilde{r}_p and \tilde{r}_s according to the following equation⁹:

$$\rho = \frac{\tilde{r}_p}{\tilde{r}_s} = \tan(\Psi) e^{i\Delta} \quad (3)$$

The ellipsometer (from J.A. Woollam Company) obtains this data by sending a beam with known polarization towards the sample, and then measures the polarization of the light that reflects off the sample. The reflected light is, in general, elliptically polarized, thus giving rise to the term ellipsometry. The measured polarization of the reflected light is in turn used to find the Ψ and Δ parameters by comparing it to the light's initial known polarization.

Specifically, Ψ is the tilt of the major axis of the polarization ellipse relative to the s -plane, and Δ is related to the eccentricity of the ellipse. These values can then, once analyzed with the proper model, be used to find the complex dielectric function and hence the complex conductivity.

Because ellipsometry works via reflection off of the surface of the sample, care must be taken to avoid having reflections from the backside of the sample enter the detector, as that would have to be accounted for in the model and would complicate it. This is done by roughening the backside of the samples with diamond scouring pads, so backside reflections will be scattered and not enter the detector. The Woollam V-VASE ellipsometer operates between the range of 0.6 and 6 eV.

I.2 FTIR Spectroscopy

Fourier-transform infrared spectroscopy works on similar principles to the well-known Michelson-Morley interferometer and will be used in the infrared range. A modulated beam containing many frequencies of light, known as an interferogram, is transmitted through the sample, and after it is detected, a Fourier transform is applied to the intensity measurements in order to obtain a broadband spectrum. This therefore allows for much quicker and more thorough measurement over a wider range of frequencies than more traditional spectroscopic methods that use discrete measurements, and works between the range of 1 meV and 2.5 eV.

For the measurements in this experiment, the mid-infrared source was used to provide intensity between 0.2 eV and 0.8 eV. Below 0.2 eV, the lanthanum aluminate substrate becomes opaque, so transmission measurements are not possible.

I.3 Techniques for Modeling the Complex Dielectric Function

Current techniques for modeling the complex dielectric function start with appropriate models of the observed phenomena. Phonons are typically modeled using a Lorentzian oscillator, which has the following form:

$$\hat{\epsilon}(\omega)_{Lorentz} = 1 + \sum_n \frac{Amp}{\omega_n^2 - \omega^2 - iBr_n\omega} \quad (4)$$

In this equation, ω_n is the center frequency of each phonon oscillator, Amp is the amplitude, and Br_n is the broadening parameter. This oscillator model comes from a model which treats the material as if the atoms were connected by springs and formed a harmonic oscillator, and the incoming electric field of the photons is treating as a driving force. In the Lorentzian lineshape, the amplitude is the area underneath the curve, ω_n denotes the position of the maximum, and Br_n the full-width half-max.

Lorentzian oscillators can also be used to model interband transitions in a material¹⁰. In this case, the atom is treated as a quantum two-level system, with the following wavefunction:

$$\Psi(\vec{r}, t) = \Psi_0 e^{-\frac{iE_0 t}{\hbar}} + \sum_l a_l(t) \Psi_l e^{-\frac{iE_l t}{\hbar}} \quad (5)$$

Where Ψ_0 is the ground state, and the various Ψ_l are the excited states, and $a_l(t)$ are some coefficients that will be determined via the Schrodinger equation:

$$i\hbar \frac{\partial}{\partial t} \Psi(\vec{r}, t) = -(H_0 + H') \Psi(\vec{r}, t) \quad (6)$$

With the incoming electric field as a perturbation to the Hamiltonian, $H' = e\vec{E} \cdot \vec{r}$.

By using perturbation theory and Fermi's golden rule $T_{g \rightarrow e} = \frac{2\pi}{\hbar} |\langle e|H'|g\rangle|^2 \rho$, the forms of the a_l coefficients can be extracted, and are found to be:

$$a_l(t) = \frac{\vec{E}}{2\hbar} \left(\frac{1 - e^{\frac{i(\hbar\omega + E_l - E_0)t}{\hbar}}}{\hbar\omega + (E_l - E_0)} - \frac{1 - e^{\frac{i(-\hbar\omega + E_l - E_0)t}{\hbar}}}{\hbar\omega - (E_l - E_0)} \right) \int \Psi_l^*(-e\vec{r})\Psi_0 d\vec{r} \quad (7)$$

Where E_l is the energy associated with each particular level, and $\int \Psi_l^* e\vec{r}\Psi_0 d\vec{r} = er_{l0}$ is the dipole matrix element. The polarization is given by

$$\vec{P} = \langle -e\vec{r}(t) \rangle = \int \Psi^*(\vec{r}, t)(-e\vec{r})\Psi(\vec{r}, t)d\vec{r} = \alpha\vec{E} \quad (8)$$

By using the formula $\varepsilon_1 = 1 + 4\pi N\alpha(\omega)$ and the Kramers-Kronig relation, the following dielectric constants are obtained for a single level:

$$\hat{\varepsilon}(\omega) = 1 + \frac{4\pi Ne^2}{m} f_{10} \left[\frac{1}{\omega_{10}^2 - \omega^2} + \frac{i\omega}{2\pi} \delta(\omega^2 - \omega_0^2) \right] \quad (9)$$

Where the oscillator strength is defined as $f_{10} = \frac{2m}{\hbar^2} \hbar\omega_{10}|r_{10}|^2$. This gives a delta function in ε_2 at the oscillator energy ω_{10} , but in a real crystal this is not seen, and there is instead some broadening. The simplest model for the broadening is the Lorentzian, which gives the following form:

$$\hat{\varepsilon}(\omega) = 1 + \frac{4\pi Ne^2}{m} \frac{f_{10}}{(\omega_{10}^2 - \omega^2) - \frac{i\omega}{\tau}} \quad (10)$$

However, a better control of the shape of the broadening is often needed, and there are a number of possible alternative models for the broadening component. One of these is the Tauc-Lorentz model, which models the fact that transitions are more likely to be excited above the bandgap energy, and so incorporates a bandgap energy E_{g_n} below which transitions are not excited. Multiple interband transitions are similarly treated as

further terms in a series, similar to how multiple phonons are treated. The Tauc-Lorentz model's $\varepsilon_{2,n}$ terms are as follows, with $\varepsilon_{1,n}$ calculated using the Kramers-Kronig relation.

$$\varepsilon_{2,n} = \begin{cases} \frac{Amp_n\omega_n C_n(\omega - Eg_n)^2}{(\omega^2 - \omega_n^2)^2 + C_n^2\omega^2} \cdot \frac{1}{\omega} & \omega > Eg_n \\ 0 & \omega \leq Eg_n \end{cases} \quad (11)$$

To remain physical ($\varepsilon_2 \geq 0$), the broadening C_n and the gap energy Eg_n must be constrained such that $C_n < 2\omega_n$, and $Eg_n < \omega_n$.⁹

In metals, the increased ability of electrons to move in the material suggests a different model, known as the Drude⁹. In this model, the motion of the electrons is treated as relatively free, but having some relaxation time τ . In the absence of an incoming photon, therefore, the equations of motion look as follows:

$$\frac{d\langle\vec{p}\rangle}{dt} = -\frac{\langle\vec{p}\rangle}{\tau} \quad (12)$$

Thus, when the electric field of the photon is added, the equation of motion for the momentum looks as follows:¹⁰

$$\frac{d\langle\vec{p}\rangle}{dt} = -\frac{\langle\vec{p}\rangle}{\tau} - e\vec{E} \quad (13)$$

From this equation of motion, a current density \vec{J} can be obtained via the equation $\vec{J} = -Ne\vec{p}/m$, with N being the density of charge carriers, e the electronic charge, and m the carrier mass. From this, the conductivity can be obtained using the Ohm's law relation $\sigma = \vec{J}/\vec{E}$. With an oscillating electric field $\vec{E}(t) = \vec{E}_0 e^{-i\omega t}$ this takes on a complex form $\hat{\sigma}$, and the complex conductivity is related to the complex dielectric function via the following equation:

$$\hat{\varepsilon} = 1 + \frac{4\pi i}{\omega} \hat{\sigma} \quad (14)$$

Finally, this can now be used to obtain the Drude model for absorption in a metal in terms of the complex dielectric function:

$$\hat{\epsilon}(\omega)_{Drude} = 1 - \frac{\omega_p^2}{\omega^2 - \frac{i\omega}{\tau}} \quad (15)$$

Here ω_p is the plasma frequency of the material, and is a function of the density of particles and their mass. It can be seen that the Drude model of conduction has the form of a Lorentzian oscillator with a broadening of $1/\tau$ centered at the origin. The equivalent form used in the analysis incorporates the resistivity ρ .⁹

$$\hat{\epsilon}(\omega)_{Drude} = 1 - \frac{\hbar}{\epsilon_0 \rho (\tau \cdot \omega^2 + i\hbar)} \quad (16)$$

II. Experimental Procedure

It was first necessary to characterize the complex dielectric function of the LAO substrate using the ellipsometer and the FTIR spectrometer. This data was then used in the modeling of the manganite film. Measurements were taken across a variety of temperatures in order to determine how the substrate properties change with temperature, and it was found that these changes were minor, as expected.

Once this data was taken, the same measurements were taken of the film-substrate system at a variety of temperatures between room temperature and 400K for both annealed and unannealed films. By comparing these data sets, how annealing impacts the temperature dependence and the optical properties of LSMO can be better understood.

To measure temperature dependence, it was first necessary to build and solder two cables, one to connect a thermometer to the LakeShore 335 temperature controller, and one to attach a 50 Ω aluminum heater to the temperature controller. This allowed the temperature to be controlled directly. Prior to data collection, the ellipsometer was

calibrated using a reflective SiO₂/Si wafer of known properties. All samples were mounted to the heater using GE varnish, which allows the heat to be transferred to the substrate, while still allowing the substrate to be removed after the data was collected.

For the collection of transmission data, the Bruker Vertex 80v FTIR spectrometer was used. This device is constantly kept in vacuum to prevent water vapor in the atmosphere from interfering with the spectrum or the delicate optics of the machine. Therefore, a second cable had to be constructed, soldered, and tested, this one attached to a hermetically sealed vacuum connector mounted to the spectrometer via a custom part. This allowed the temperature controller to interface with the heater, for which the same 50 Ω resistor was used as was in the ellipsometer measurements. On the FTIR itself, all measurements were taken with a 1.5mm aperture spot size and using the liquid-nitrogen cooled MCT detector.

The lanthanum aluminate single crystal substrate with (100) orientation was roughened on the backside with a diamond scouring pad to prevent back reflections from affecting the ellipsometry measurement, and then measured with calipers to have a thickness of 0.5mm. Three sets of data were taken at 297K (room temperature), 420K, and 360K, in that order. This data is shown in Figure 4.

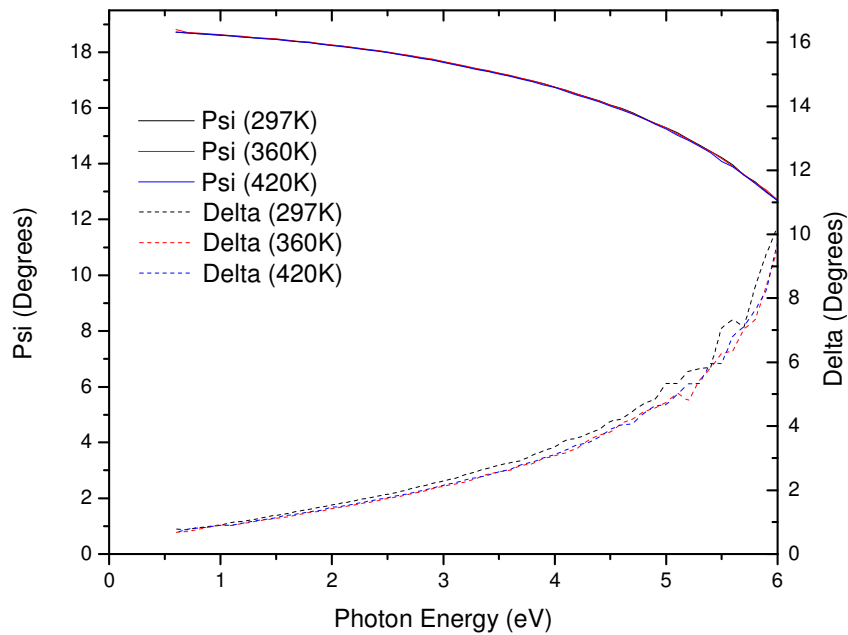


Figure 4: Ellipsometric coefficients of lanthanum aluminate at 75 degrees showing the small temperature dependence.

As can be seen, the temperature dependence is not particularly strong. This was initially modeled in the Woollam WVASE analysis software with a single Tauc-Lorentzian oscillator, using the software's General Oscillator (GenOsc) feature. Additionally, a pole oscillator was used to model potential features above the range of data.

Next, transmission measurements were taken on a second sample of LAO in which both sides of the substrate are smooth. By using a translator attached to the heating stage, raw measurements were taken of a through-hole and the sample, and the second spectrum was divided by the first to obtain the absolute transmission. Two data sets at 20 degree temperature intervals were taken and were averaged for improved accuracy. The resulting data set used for the modeling is shown in Figure 5. This data is consistent with prior transmission measurements taken of LAO.¹¹

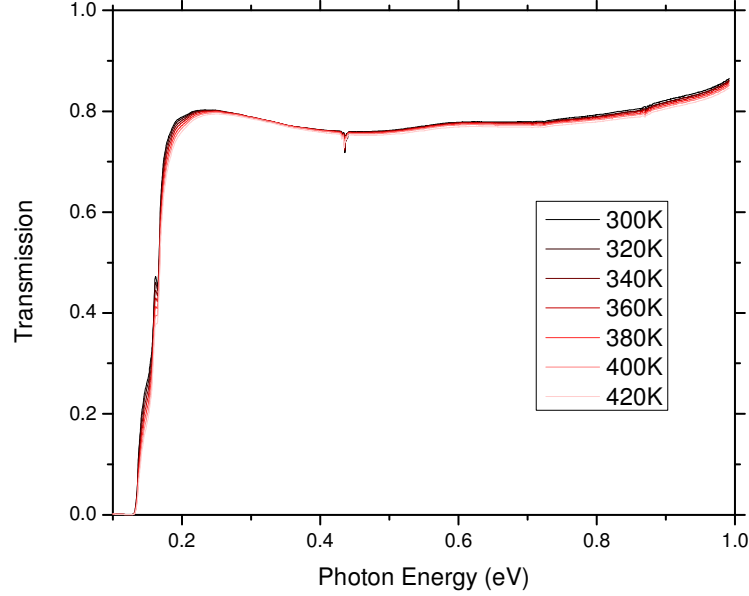


Figure 5: Transmission data collected on LAO at various temperatures.

III. Analysis of the Substrate

The high energy features in Figure 4 were modeled well with a Tauc-Lorentzian oscillator. However, the rapid fall-off seen in transmission data below 0.2 eV comes from the phonons of the material. To model these phonons, as a starting point the phonon oscillators described by Z.M. Zhang, et.al. were used¹¹. However, these phonons still did not accurately describe the rapid fall-off. Zhang suggested but did not use a method proposed by Barker in 1964 to examine the phonons of MgF_2 and ZnF_2 .¹² This method modified the traditional Lorentzian model of phonon absorption, seen below in the form used by Zhang:

$$\hat{\epsilon}(\omega) = 1 + \sum_n \frac{S_n \omega_n^2}{\omega_n^2 - \omega^2 - iBr_n \omega} \quad (17)$$

In this equation, ω_n is the center frequency of each phonon oscillator, S_n is the strength, and Br_n is the broadening parameter. According to Barker, this broadening

parameter is in a real crystal not merely a constant, but should have a more rapid fall-off, which is similar to the effect seen in the LAO transmission data. Barker proposed modeling it by adding an exponential decay term to the broadening above some frequency ω_0 . The following equations show an oscillator modeled in this way:

$$\hat{\varepsilon}(\omega) = 1 + \sum_n \begin{cases} \frac{S_n \omega_n^2}{\omega_n^2 - \omega^2 - iBr_n \omega} & (\omega < \omega_0) \\ \frac{S_n \omega_n^2}{\omega_n^2 - \omega^2 - iBr_n \omega e^{-\frac{\omega}{\omega_0 d} + \frac{1}{d}}} & (\omega > \omega_0) \end{cases} \quad (18)$$

Added to the equation is the characteristic frequency ω_0 and d , a damping parameter that can be adjusted to control the rate of the fall-off. The values from Zhang's paper were used to for the basic parameters of the Lorentzian; ω_0 and d were determined through fits to the data. A close eye was kept on the generated reflectance data to make sure it was consistent with actual results found by Zhang and others.

For the temperature dependence, a paper by P. Calvani found the positions of the phonons for 25K and 300K.¹² The trends were linearly interpolated to 400K, which was then used as an upper bound for determining the software fit. Once the fit at 400K was finalized, interpolation was used to fit to the data sets at intermediate temperatures. The ellipsometric data for values other than room temperature and 360K was interpolated from those two data sets and the data taken at 420K. As the temperature dependence was extremely small to begin with, this was seen as an accurate procedure.

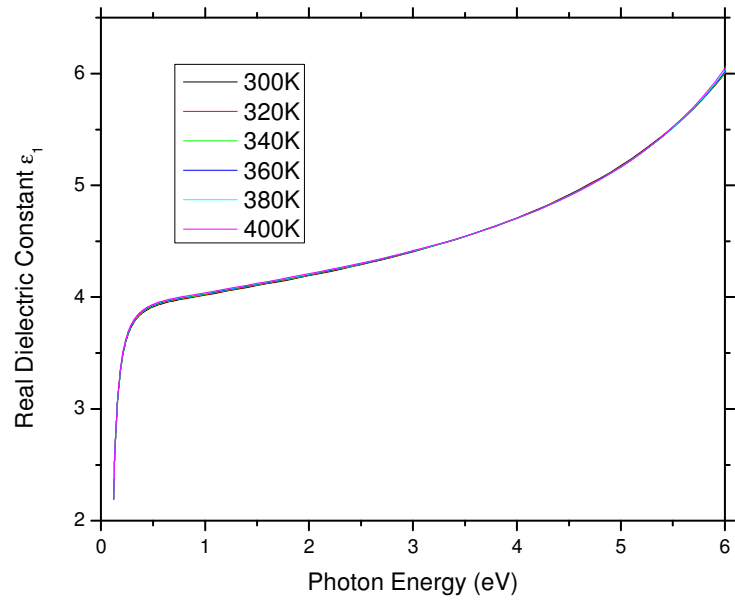


Figure 6: Real dielectric constant of LAO at various temperatures. The small temperature dependence can again be seen.

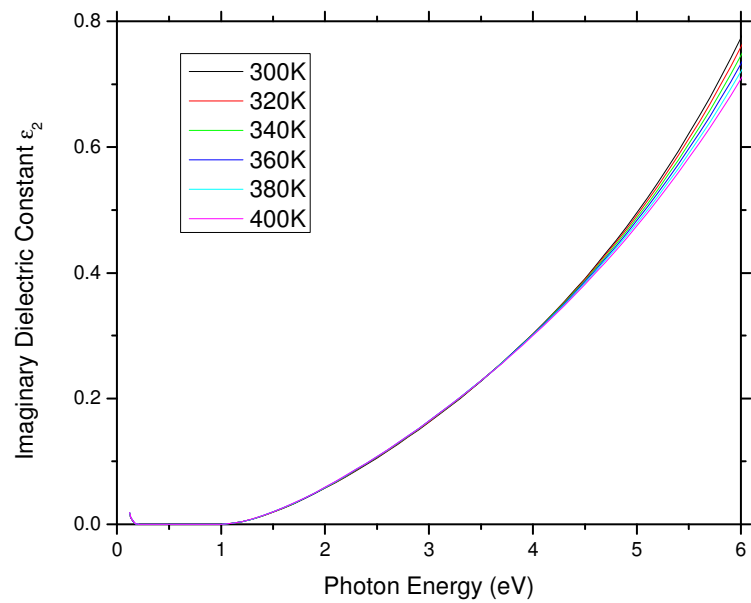


Figure 7: Imaginary dielectric constant of LAO at various temperatures. The small temperature dependence can again be seen.

IV. Data collection on the Film-Substrate System

Two films grown by collaborators at Towson University were used, one annealed in an O_2 atmosphere after growing. The unannealed sample measured 1cm x 1cm, while the annealed sample measured 1cm by 0.6cm. With both the annealed and unannealed LSMO films, transmission measurements were taken first, before any roughening of the backside of the substrate was done. These were taken in an identical way to the LAO transmission, using the translator to allow absolute transmission measurements. Data was taken in intervals of 20K between 300K and 400K, and each data set was the average of at least three spectroscopic scans with the FTIR. The low and high temperature states for both samples can be seen in Figure 8.

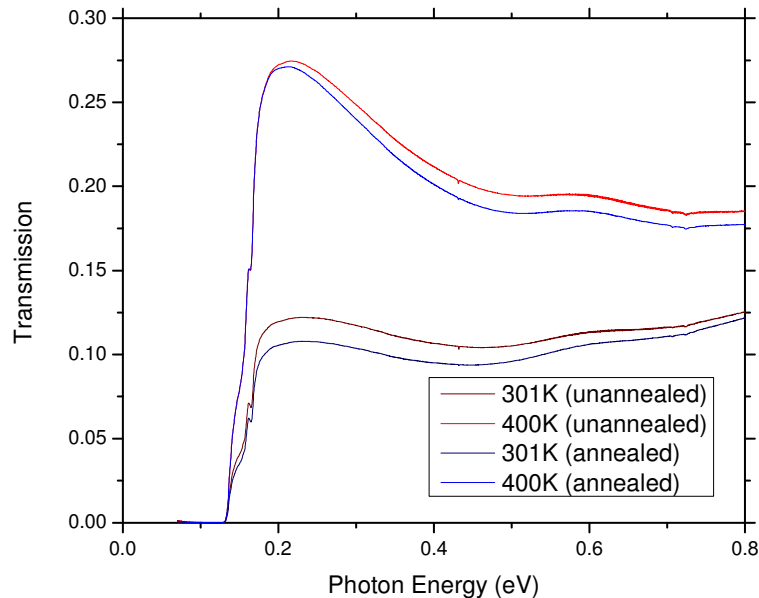


Figure 8: Transmission data for annealed and unannealed LSMO thin films on LAO. The metallic phase at 300K has a lower transmission than the insulating phase at 400K, and the annealed sample shows lower transmission at all temperatures.

Following this, the backsides of the two samples were roughened such that while the backside of part of the sample was roughened for ellipsometry, another section, not used in the measurement, was kept smooth. On the ellipsometer, data for the two samples was taken at 75° and 60° angles of incidence at room temperature (300K), at 60° for 20K intervals, and then once 400K was reached, both 75° and 60° data was again taken. This process was done first with the annealed sample, and then was repeated to obtain the temperature dependence of the unannealed sample. The annealed data at 60° is shown in Figures 9 and 10, while the unannealed data at 60° is shown in Figures 11 and 12.

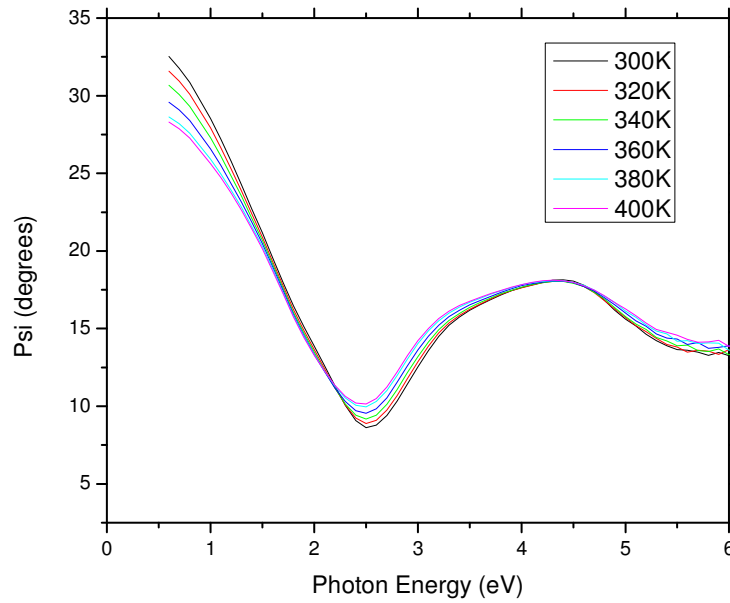


Figure 9: Temperature-dependent Ellipsometric data for annealed LSMO at 60 degree angle of incidence.

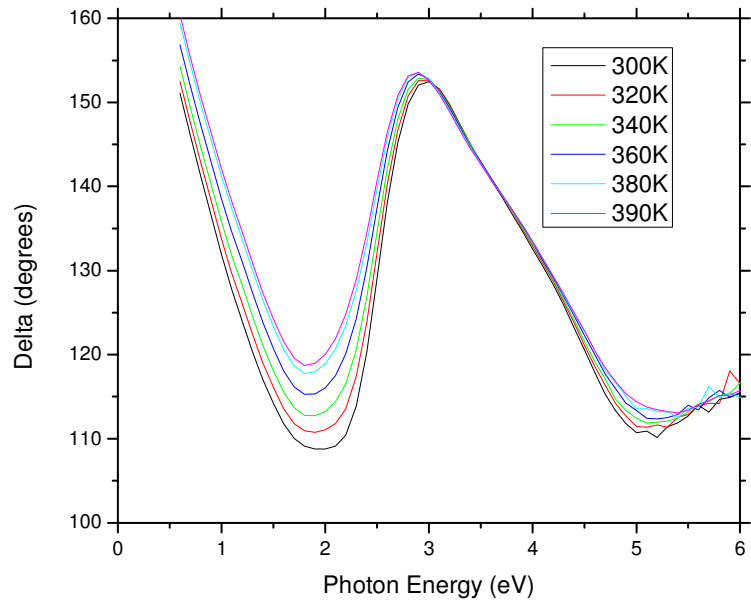


Figure 10: Temperature-dependent Ellipsometric data for annealed LSMO at 60 degree angle of incidence

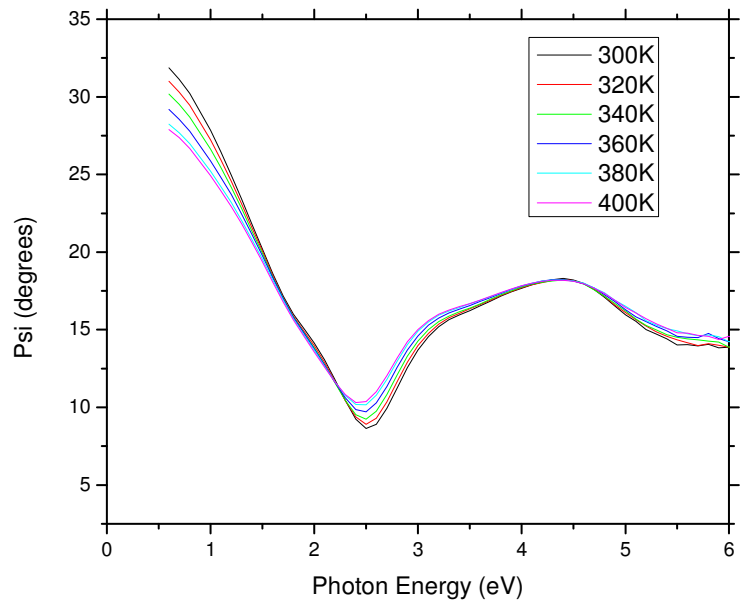


Figure 11: Temperature-dependent Ellipsometric data for unannealed LSMO at 60 degree angle of incidence. A new feature can be seen at about 2 eV that is not present in the annealed sample.

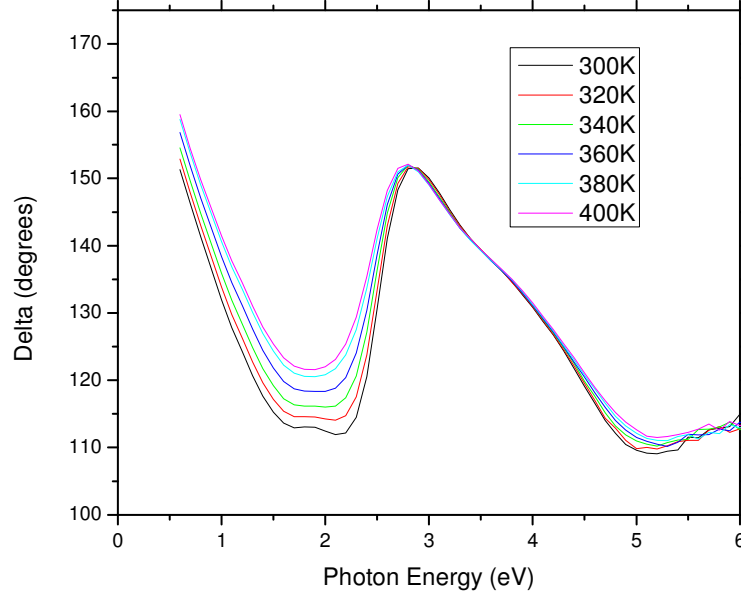


Figure 12: Temperature-dependent Ellipsometric data for unannealed LSMO at 60 degree angle of incidence. A new feature can be seen at about 2 eV that is not present in the annealed sample.

V. Data Modeling and Analysis

The GenOsc model was again used to model the LSMO thin films. Metallic behavior was modeled using the Drude model, and it was observed that above 360K, the Drude conduction was no longer necessary in both the annealed and unannealed data. Both films were modeled in $\hat{\epsilon}$, which was then used to obtain the complex conductivity $\hat{\sigma}$.

The real part of the conductivity σ_1 obtained from these models can be seen in Figure 13 for the annealed sample and Figure 14 for the unannealed sample, and the imaginary part σ_2 in Figures 15 and 16.

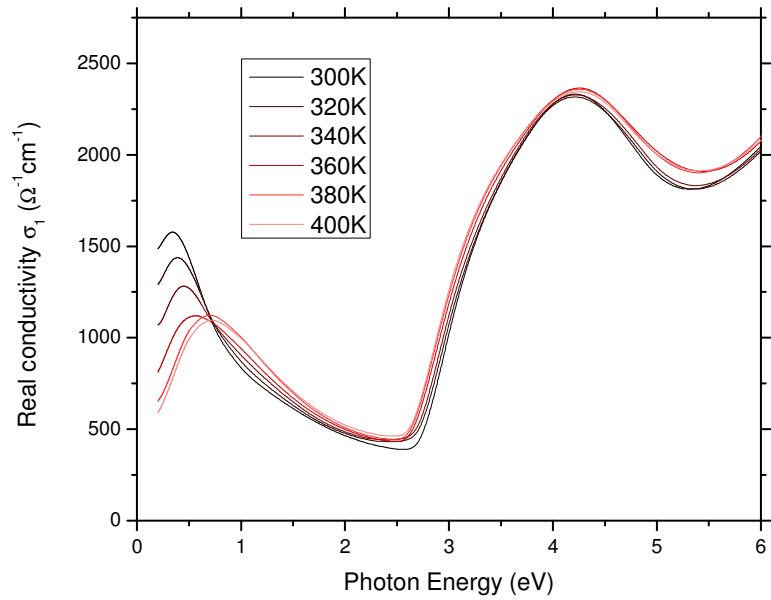


Figure 13: Temperature-dependent conductivity of annealed LSMO. The phase transition can be seen in the low-energy limit.

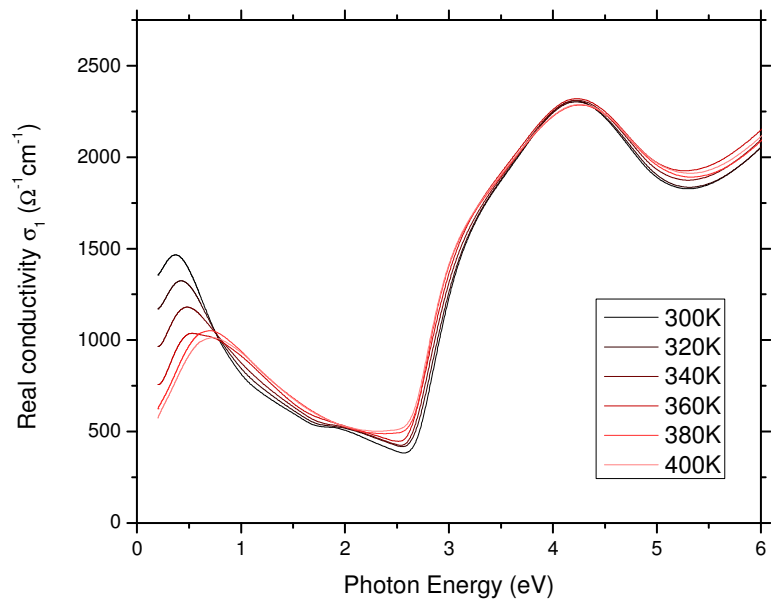


Figure 14: Temperature-dependent real conductivity of unannealed LSMO. The phase transition can be seen in the low-energy limit, and the feature at 2 eV is also present.

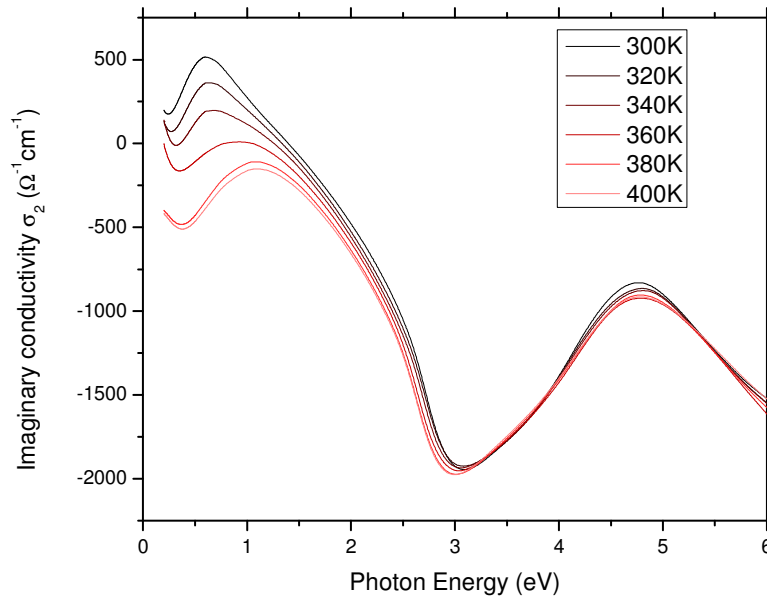


Figure 15: Temperature-dependent imaginary conductivity of annealed LSMO.

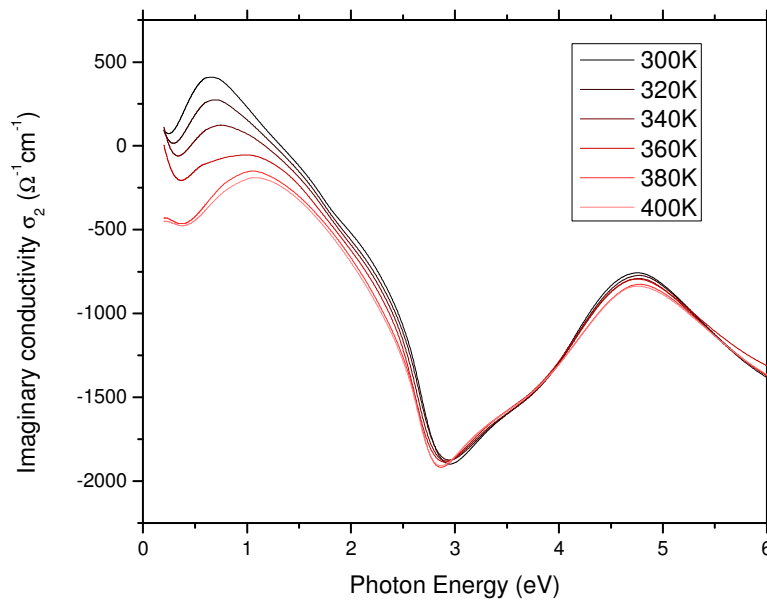


Figure 16: Temperature-dependent imaginary conductivity of unannealed LSMO.

It can be seen that the graphs have similar shapes for annealed and unannealed films. However, approaching the DC limit the annealed sample shows a higher

conductivity, as would be expected for an annealed film. The conductivities at 0.2 eV, the lowest energy measured, are shown in Figure 17. From this it can be seen that rather than raising the conductivity across the board, the annealing has likely increased T_c . The two lines approximately overlap via a translation in the temperature axis of about 10K. The data also shows the gradual reduction in conductivity with temperature that would be expected due to phase separation during the metal-insulator transition.⁵

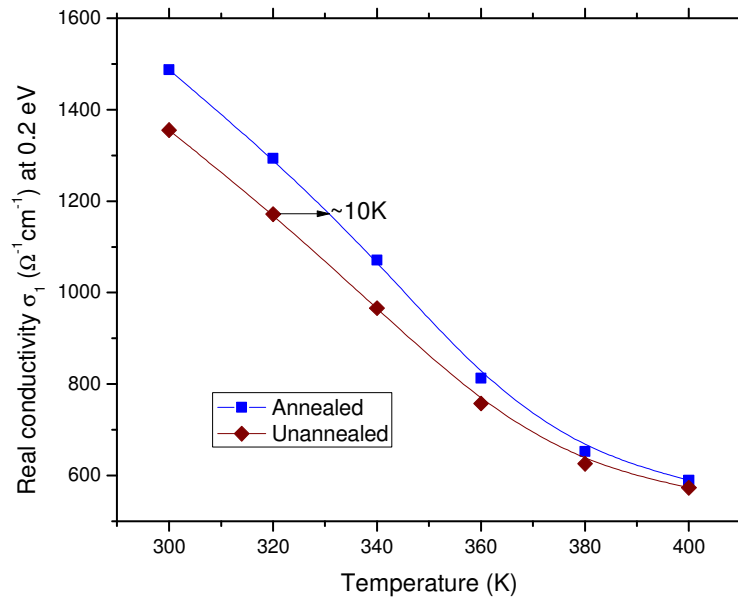


Figure 17: Conductivity at 0.2 eV, the lowest energy measured, as a function of temperature. By comparing the curves for the annealed and unannealed sample, it can be seen that T_c is shifted by 10K.

Interestingly, in both cases measured conductivities are generally higher than those reported by Quijada et. al.'s 1998 paper on manganite thin films. In Figure 18, the annealed and unannealed data in the insulating phase at 400K is shown.

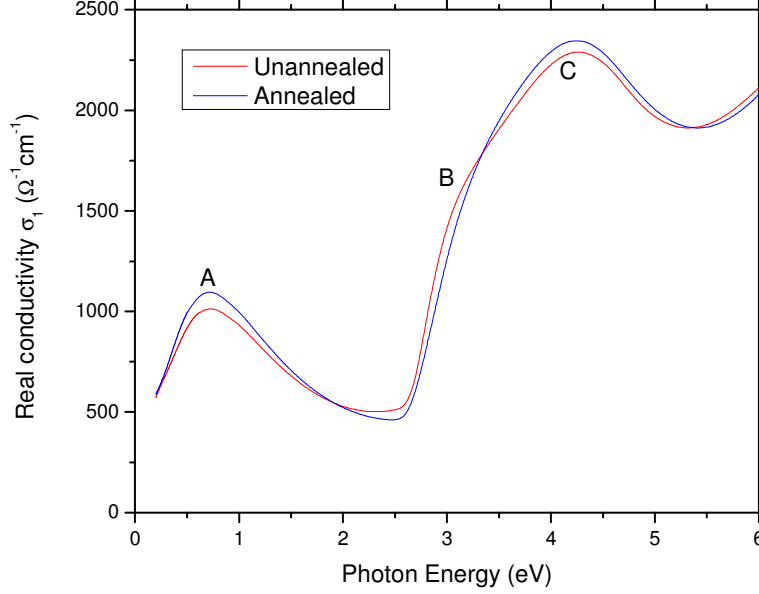


Figure 18: 400K conductivities for annealed and unannealed films with significant features labeled.

The feature just below 1eV, at the point labeled A, likely corresponds with the transition between e_g states in adjacent manganese ions². As can be seen in Figure 1, for a bound electron in the lower Jahn-Teller split state to move into an unoccupied e_g level requires some energy input $E_{JT} \approx 1\text{eV}$. This feature would not be expected to be present in the metallic state, where electrons can move freely between e_g states of adjacent ions.

There is a second feature at the point labeled B, at about 3 eV. This likely corresponds to transitions similar to those at 1 eV, but where the spin of the electron is antiparallel to the destination ion's t_{2g} electrons². This can occur in the insulating phase because the material is no longer ferromagnetic and the t_{2g} spins on adjacent ions are not necessarily aligned. It appears to be stronger in the unannealed sample, possibly because of increased spin-flip scattering. The energy of this feature should be the sum of the energy required to excite a bound electron and the Hund's coupling energy J_H .

The dominant feature at the point labeled C, about 4 eV, likely corresponds to transitions between the oxygen O_{2p} levels and the e_g levels. A peak is also seen at this region in the conductivity of the parent compound, LaMnO_3 , and has been assigned to $O_{2p} \rightarrow e_g$ optical transitions.¹⁴ Next we turn our attention to the 300K metallic phase data, as seen in Figure 19.

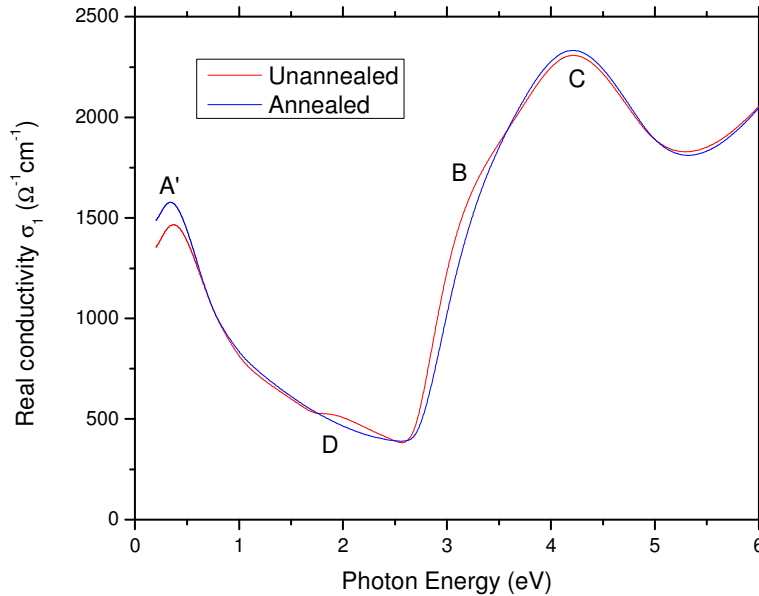


Figure 19: 300K conductivities for annealed and unannealed films with significant features labeled.

Here the A' feature is seen and occurs at lower energy compared to the feature in the insulating phase. However, this is likely due to phase separation and the presence of domains of the insulating phase even at 300K, as was observed by Becker⁵. The A' feature therefore comes from the combination of the A feature of the insulating phase and Drude conduction in the metallic phase. The continued presence of the feature at B is likely also due to this phase separation. The feature at C, the $e_g \rightarrow O_{2p}$ transition, can occur in the metallic phase as well as in the insulating phase.

There is a slight but clearly noticeable feature in the unannealed sample at the point labeled D at 2 eV, which disappears in the annealed sample. A possible explanation of this feature is that it arises from the disorder in the lattice caused by oxygen deficiency. In a typical ferromagnetic state, spin flip transitions between e_g levels of adjacent ions are not possible as all the spins are aligned, and optical transitions preserve spin. However, an increased scattering rate caused by disorder could cause some spins to become antialigned. For this transition to occur, it would need to be excited with the Hund's coupling energy $J_H \approx 2$ eV. Given the presence of the A feature at ~ 1 eV, and the B feature from antialigned spin transitions in the insulating phase at ~ 3 eV, a J_H of ~ 2 eV is consistent with the data. Other estimates of J_H for LSMO place it within the same range, at ~ 2.5 eV.¹⁵

VI. Conclusions

In this project, ellipsometric and spectroscopic transmission data was taken for the substrate material, lanthanum aluminate, and annealed and unannealed thin films of $\text{La}_{0.67}\text{Sr}_{0.33}\text{MnO}_3$ grown on said substrate. This data was used to obtain the frequency dependent complex dielectric function and hence the complex conductivity as a function of temperature in the annealed and unannealed samples. The broadband infrared and optical data allowed us to gain a new perspective of how the properties of this material can be controlled and manipulated.

It was found that by increasing the oxygen content using the annealing process, T_c and low frequency conductivity increased. The increase in T_c was approximately 10K. The magnitude of the Jahn-Teller energy splitting was deduced to be ~ 1 eV. Reduced oxygen content as seen in the unannealed sample was also observed to introduce a feature

in the complex conductivity, possibly due to strain and disorder. This feature allowed us to directly estimate Hund's coupling J_H in the material to be ~ 2 eV.

Acknowledgements

I would like to thank first my research advisor, Prof. Mumtaz Qazilbash, as well as all the people I collaborated with at William and Mary, including graduate students Peng Xu and Tyler Huffman, whose help with calculations and modeling was invaluable, as well as my fellow undergraduates Arlo Hollingshad and Nick Penthorn, who designed and built some of the experimental apparatus used. Additionally, I would like to thank Raj Kolagani and Vera Smolyaninova from Towson University, who grew and characterized the films used in this experiment. Without the help of all of these people, this thesis would not have been possible.

References

- [1]. A.J. Millis, *Lattice effects in magnetoresistive manganese perovskites*. Nature **392**, 147-150 (1998).
- [2]. M. Quijada, J. Černe, J.R. Simpson, H.D Drew, K.H. Ahn, A.J. Millis, R. Shreekala, R. Ramesh, M. Rajeswari and T. Venkatesan, “*Optical conductivity of manganites*”, Physical Review B **58**, 16093-16102 (1998).
- [3]. A.V. Boris, N.N. Kovaleva, A.V. Bazhenov, P.J.M. van Bentum, Th. Rasing, S-W. Cheong, A.V. Samoilov, and N.-C. Yeh, “*Infrared studies of a $La_{0.67}Ca_{0.33}MnO_3$ single crystal*”, Physical Review B **59**, R697-R700 (1999).

- [4] J. Hemberger, A. Krimmel, T. Kurz, H.-A. Krug von Nidda, V. Yu. Ivanov, A. A. Mukhin, A. M. Balbashov and A. Loidl, “*Structural, magnetic, and electrical properties of single-crystalline $La_{1-x}Sr_xMnO_3$ ($0.4 < x < 0.85$)*”, *Physical Review B* **66**, 094410-1-8 (2002).
- [5]. T. Becker, C. Streng, Y. Luo, V. Moshnyaga, B. Damaschke, N. Shannon, K. Samwer, “*Intrinsic Inhomogeneities in Manganite Thin Films Investigated with Scanning Tunneling Spectroscopy*”, *Physical Review Letters* **89**, 237203 (2002).
- [6]. T. Li, B. Wang, H. Dai, Y. Du, H. Yan, Y. Liu, “*Annealing effect on the structural and magnetic properties of $La_{0.7}Sr_{0.3}MnO_3$ films.*”, *Journal of Applied Physics* **98**, 123505- (2005).
- [7]. J. Dho, N.H. Hur, I.S. Kim, Y.K. Park, “*Oxygen pressure and thickness dependent lattice strain in $La_{0.7}Sr_{0.3}MnO_3$ films*”, *Journal of Applied Physics* **94**, 7670 (2003).
- [8]. V. N. Varyukhina, Yu. V. Medvedeva, Yu. M. Nikolaenko, A. B. Mukhina, B. V. Belyaev, V. A. Gritskikh, I. V. Zhikharev, S. V. KaraMurzab, N. V. Korchikov, and A. A. Tikhiib, “*Conductivity of $La_{0.7}Sr_{0.3}MnO_{3-\delta}$ Films with Small Deviations from Stoichiometry with Respect to Oxygen*”, *Technical Physics Letters* **35**, 937-940 (2009).
- [9]. J.A. Woollam Company, Inc., *Guide to Using WVASE32*, (J.A. Woollam Co., Inc., Lincoln, NE, 2010).
- [10] M. Dressel and G. Grüner, *Electrodynamics of Solids: Optical Properties of Electrons in Matter*, Cambridge University Press, 2002.
- [11]. Z.M. Zhang, B.I. Choi, M.I. Filk, “*Infrared refractive indices of $LaAlO_3$, $LaGaO_3$, and $NdGaO_3$* ”, *Journal of the Optical Society of America* **11**, 2252-2257 (1994).

- [12]. A.S. Barker, “*Transverse and Longitudinal Optic Mode Study in MgF₂ and ZnF₂*”, Physical Review **136**, 1290-1295 (1964).
- [13]. P. Calvani, M. Capizzi, F. Donato, P. Dore, S. Lupi, P. Maselli, C.P. Varsamis, “*Infrared optical properties of perovskite substrates for high-T_c superconducting films*”, Physica C **181**, 289-295 (1991).
- [14]. T. Arima, Y. Tokura, J.B. Torrance, “*Variation of optical gaps in perovskite-type 3d transition metal oxides*”, Physical Review B **48**, 17006-17009 (1993).
- [15]. M. Cesaria, A. P. Caricato, G. Maruccio, M. Martino, “*LSMO – growing opportunities by PLD and applications in spintronics*”, J. Phys.: Conf. Ser. **292**, 012003 (2011).